J Mater Sci (2016) 51:4451–4461
DOI 10.1007/s10853-016-9757-2

Reversible metallization of SnO_2 films under hydrogen and oxygen containing atmospheres

P. M. Desimone[1] · C. G. Díaz[1] · J. P. Tomba[1] · C. M. Aldao[1] · M. A. Ponce[1]

Received: 31 August 2015 / Accepted: 16 January 2016 / Published online: 1 February 2016

Abstract The adsorption of different gases onto tin oxide films surfaces promotes electrical conductance variations. Films chemiresistive properties depend on the intergranular barrier heights and on the concentration of non-stoichiometric defects that, in the case of tin oxide, are mainly oxygen vacancies. We found that film exposures to an H_2-containing atmosphere over 400 °C led to unusual results that cannot be explained resorting to regular interpretations. By means of Raman spectroscopy and XRD characterization, we show that, at high enough temperatures, when films are exposed to hydrogen, the tin dioxide converts into tin monoxide and metallic tin. Then, when films are exposed to air atmosphere, the oxygen diffuses into the grains converting the metallic tin back into tin dioxide. These findings are consistent with electrical measurements.

Introduction

Tin oxide is the most common metal oxide semiconductor used as a sensor material for diverse gases [1–5]. The presence of gases can be detected through changes in the film conductivity. It is well established that tin oxide is a wide band-gap (3.6 eV) semiconductor of *n*-type due to oxygen deficiency. Also, it is well known that oxygen can be chemisorbed at grains surfaces as charged species affecting intergranular potential barriers that control the film conductivity [1–5]. Thus, the sensing mechanism is mainly based on the surface reactions that involve chemisorbed species [6–8]. It is generally accepted that barriers formed between grains are responsible for the sensor conductivity and that they have a Schottky-type nature [2]. Researchers have regularly considered a conductance of the type

$$G = G_0 \exp(-eV_s/kT), \quad (1)$$

where V_s is the band bending, T the temperature, and k the Boltzmann constant. Equation (1) reflects an activated process due to intergranular barriers.

In previous work, we have proposed that at temperatures high enough ($>\sim 200$ °C) the adsorbed oxygen onto the surface can diffuse into the grains, annihilating oxygen vacancies, and thus reducing the donor concentration [9]. Conversely, if oxygen diffuses out of the grains, vacancies are formed. Under equilibrium, these processes cancel each other. However, if films are treated with a reducing reagent such as H_2, the amount of adsorbed oxygen would be reduced and therefore the oxygen diffusion into the grains. Thus, oxygen migration from the bulk to the surface would be accompanied with an increase of the density of oxygen vacancies.

We found that treatments with a H_2-containing atmosphere over 400 °C led to unusual results that challenge the above interpretation. In order to elucidate the consequences of exposing the films to a reducing atmosphere at high temperature, we carried out Raman and x-ray diffraction (XRD) characterization. The study was performed on samples with different grain sizes at different temperatures and thermal treatments. Measurements of electrical conductance as a function of temperature during heating and cooling of SnO_2-thick films in an oxygen containing atmosphere are also presented. Interestingly, we found that

✉ P. M. Desimone
desimone.mariela@gmail.com

[1] Institute of Materials Science and Technology (INTEMA), University of Mar del Plata and National Research Council (CONICET), Juan B. Justo 4302, B7608FDQ Mar del Plata, Argentina

tin dioxide converts into tin monoxide and metallic tin. Conversely, when films are later on exposed to an air atmosphere, the oxygen diffuses into the grains converting the tin metallic back into tin dioxide.

Experimental

Commercial high-purity SnO_2 (Aldrich, 99.99 %, 345 mesh, 244651-500G) was ground until a medium particle size of 0.1 μm (small particle, SP). Size particle distributions of the powders were determined by the Sedigraph technique with a Micromeritics. Later, a fraction of the original Sigma-Aldrich powder was thermally treated. A calcination process carried out at 1100 °C for 2 h at oxygen atmosphere led to powders with larger particle size (LP). Then, a paste was prepared with an organic binder (glycerol) using powders SP and LP. The used solid/organic binder ratio was ½. No dopants were added. Thick, porous film samples were made by painting onto insulating alumina substrate on which electrodes with an interdigitated shape had been delineated by sputtering (Doctor Blade Technique). The insulating alumina substrates were 96 % dense. An adhesion layer consisting of 25 nm titanium was deposited and then, without breaking vacuum, a platinum film 200-nm thick was deposited over the Ti layer. For defining the interdigitated electrodes, the substrates with the metal films were placed in a home-built micromachining laser. The thick of the films was measured with a Surtronic 3+(Taylor Hobson) profilometer with a diamond stylus (radius: 1 μm).

The resulting samples were first dried at 60 °C (during 24 h in dry air atmosphere) in order to evaporate the binder, and later thermally treated in dry air atmosphere up to 380 °C (using a heating rate of 1 °C/min in order to evaporate the residual binder). When temperature was reached (380 °C), films were maintained in air for 2 h. To gain confidence in the quality of the films, XRD and Raman spectra were obtained. No traces of binder were found and films presented the same spectra than for the original powder. Films were labeled SG (film with small particle size prepared with powder SP) and LG (film with large particle size, prepared with powder LP). After this thermal treatment in dry air atmosphere, the films were kept at 450 °C for 4 h in a N_2 atmosphere with 5 % H_2.

A JEOL JSM 6460-S scanning electron microscope (SEM) was employed to analyze the surfaces and cross sections of the films. Figure 1a and b show SEM images of the films studied, which reveal their porous structure required for use as sensors. The grain size is crucial for the electrical properties, as discussed in detail previously [10, 11]. From SEM images, the average particle size of samples labeled as SG was determined to be between 50 and 125 nm, whereas for LG, particle size was between 180 and 420 nm. The average thickness of both films was 57 μm as determined from the images of their respective cross sections.

Films were characterized using XRD, with a PANalytical ẊPert PRO diffraction system employing CuKα radiation (λ = 0.1542 nm) at 40 kV as generator tension and 40 mA as generator current. The samples were scanned between 20° and 90° with a step size of 0.02°. The XRD data were analyzed using ẊPert PRO HighScore software, and the crystallographic data for each phase were taken from the literature [12].

Raman spectra were acquired at room temperature with a Renishaw in Via Reflex micro-spectrometer equipped with charge-coupled device (CCD) detector of 1024 × 256 pixels. An Ar laser line (514 nm, 50 mW) was used as the excitation source in combination with a grating of 2400 grooves/mm. A 100X (0.9 NA) Leica metallurgical objective was used in the excitation and collection paths. A neutral density filter was used to reduce the incident laser power on the sample to values of about 0.2 mW, as measured with a silicon photodiode (Coherent Inc.). Confocality was achieved by limiting the active area on the spatial CCD dimension to 3 pixels and by setting the aperture of the spectrometer slit to 20 μm. In those conditions, the sampled volume has a lateral dimension below 1 μm. The sampled depth was less than 1.5 μm, as determined by z-scanning a silicon wafer above and below its surface.

The electrical resistances of the films, previously treated in hydrogen, were measured during increasing and decreasing temperature in the range 25–230 °C at a rate of ∼5 °C/min in dry air (760 mmHg). An Agilent 3440A multimeter was used for the electrical conductance measurements. Also, after the thermal treatments, in order to analyze the superficial and bulk changes during the oxygen exposure, XRD and Raman characterization were carried out for SG and LG films.

Sensing mechanisms and electrical measurements

The oxygen exchange equilibrium between SnO_2 with the gas phase is regularly written as [13]:

$$O_{latt} \Leftrightarrow V^{++} + 2e^{-} + \frac{1}{2}O_2, \quad (2)$$

where O_{latt} is neutral oxygen at the crystal, V^{++} is a doubly ionized oxygen vacancy, e^{-} is an electron, and O_2 an oxygen molecule at the gas phase. Equation (2) implies several mechanisms, as the density of vacancies must be able to evolve to reach equilibrium (for example, after a change of the oxygen pressure or temperature). Indeed,

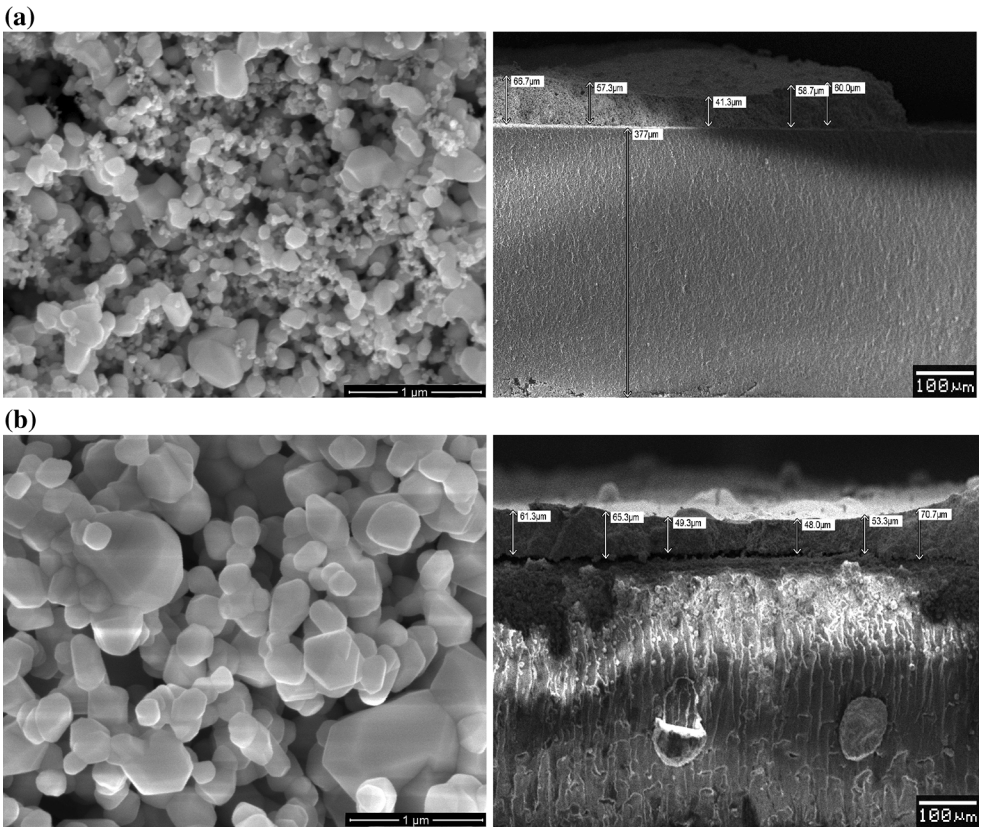

Fig. 1 Micrograph of the film showing a porous structure as required for sensor: **a** SEM micrographies of film SG, **b** SEM micrographies of film LG

neutral oxygen in the crystal leaves its position to create a doubly ionized vacancy and a doubly ionized interstitial, oxygen interstitials migrate to the surface to finally desorb to the gas phase. These reactions for oxygen can be summarized, from the gas to the bulk of the grain, as:

$$O_{2(gas)} \leftrightarrow O_{2(ads)} \leftrightarrow O^{-}_{ads} \leftrightarrow O^{-2}_{ads} \leftrightarrow O^{-2}_{int} \leftrightarrow O_{latt}, \qquad (3)$$

where $O_{2(gas)}$ refers to oxygen in the environment, $O_{2(ads)}$ to an oxygen molecule adsorbed at the grain surfaces, O^{-}_{ads} and O^{-2}_{ads} to singly and doubly ionized monatomic oxygen at the grain surface, O^{-2}_{int} to interstitial oxygen, and O_{latt} to oxygen at the tin oxide lattice [14].

Gas sensing in this type of sensors can be described based on the above mechanisms. We will assume that the temperature is such that species at grains of the sensing film can be considered in equilibrium and that the relevant bulk imperfections are interstitials anions and vacancies. The system also includes the environment where the sensor is. If the pressure is raised in a rich oxygen atmosphere, the amount of adsorbed oxygen increases and the Schottky barrier height increases. More oxygen at the surface increases the diffusion of oxygen as interstitials into the bulk establishing a new equilibrium between surface and bulk in which the amount of vacancies within grains is lower. On the other hand, if the film is treated with a reducing reagent as CO or H_2, the amount of adsorbed oxygen is reduced, the interstitial oxygen migration from the bulk to the surface becomes dominant respect to the inverse process and, therefore, the density of oxygen vacancies increases. Thus, after hydrogen treatment, an increase in oxygen vacancies can be expected. The effects on conductivity of the intergranular barrier height are easily understood as conduction is regularly described as an activated process, the thermionic emission. However, we have shown that tunneling can be dominant, and this contribution is directly related to the density of defects at the grains. Indeed, we showed that samples with similar barrier heights can present very different conductivities [15]. Impedance analysis showed that this is related to an increase in the doping, i.e., the formation of oxygen vacancies [16].

We measured electrical properties of polycrystalline SnO_2 films under a variety of thermal treatments and environments. Typical film conductance versus 1/temperature curves are presented in Fig. 2a, carried out with a film LG. Conductance was measured by raising and then lowering the temperature under an oxygen rich atmosphere,

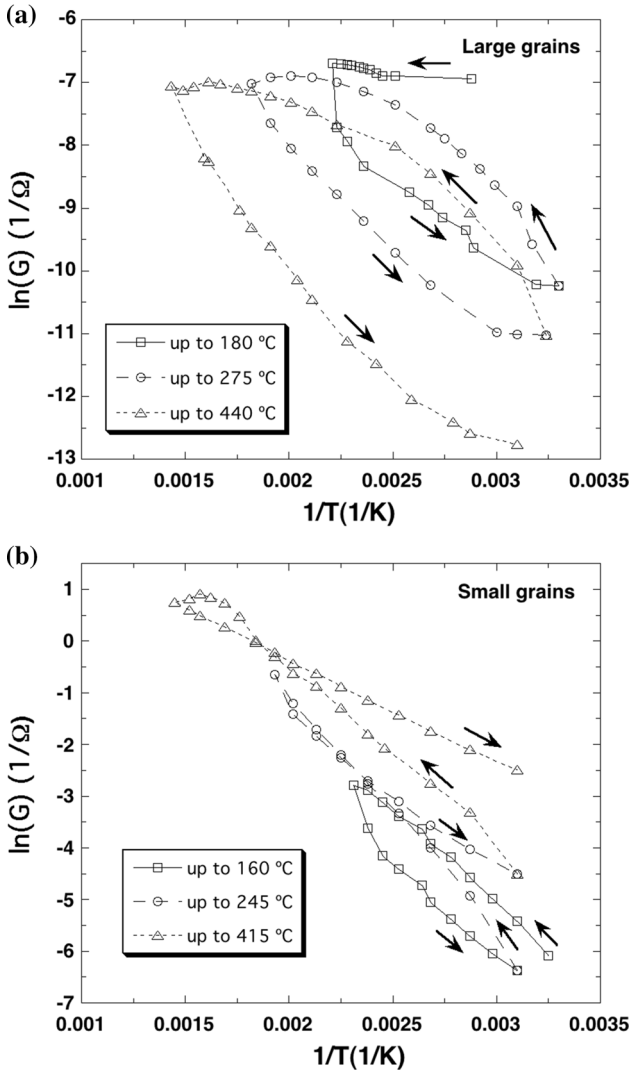

Fig. 2 Electrical conductance during heating and cooling under oxygen (8.4 mmHg) as a function of 1/temperature. **a** Films with large grains LG; **b** films with small grains SG

reaching different final temperatures. It was found that conductance after cooling was lower than after heating. This result implies higher intergranular barriers and lower density of vacancies, consistent with the oxygen exposure. Slopes as a function of temperature are around 0.53 eV [17].

Conductance versus 1/Temperature curves for a sample with small particle size (SG) are presented in Fig. 2b. For temperature ramps in a range below 160 °C, the conductivity in the cooling process is lower than in the heating process. This behavior could be associated with the oxygen adsorption in the particle surface which produces a diminution in the sample conductivity [18]. In this case, oxygen adsorption produces an increase in the potential barrier height and then a reduction in the sample conductivity is observed. At these temperatures, oxygen diffusion into the grains is not significant. Conversely, temperature ramps at which higher than 220 °C produces a final effect of increasing the sample conductivity. At these temperatures, the oxygen diffusion into the grains provokes an increase in the bottom of the overlapped barriers and, as a consequence, the conductivity increases [18]. In this case, the effective barrier height is about 0.16 eV.

We found that samples treated with hydrogen, at higher temperatures than previous reported studies, presented unexpected electrical behaviors. Figure 3 shows the conductivity during a temperature cycle in dry air, from room temperature up to 230 °C, for films SG and LG after the hydrogen treatment at 450 °C.

Films LG, having large grains, present a behavior that can be the effect of oxygen adsorption as temperature is raised, which is responsible for increasing the intergranular barriers. Curves present a very low slope, of around 0.15 eV, that could be interpreted as a consequence of narrow barriers with conduction dominated by tunneling. The conductivity in the cooling process becomes lower than in the heating process. As for results of Fig. 2, this behavior can be associated with oxygen adsorption at the grains surfaces producing a diminution of the sample conductivity. Particularly, during the cooling process, oxygen adsorption at higher temperatures produces an increasing in the potential barrier height and then a reduction in the sample conductivity. Also, at relatively low temperatures, oxygen can diffuse into the grains annihilating oxygen vacancies and thus lowering the conductivity.

Similarly to films LG, after a temperature cycle, SG conductance is lower. However, results show a

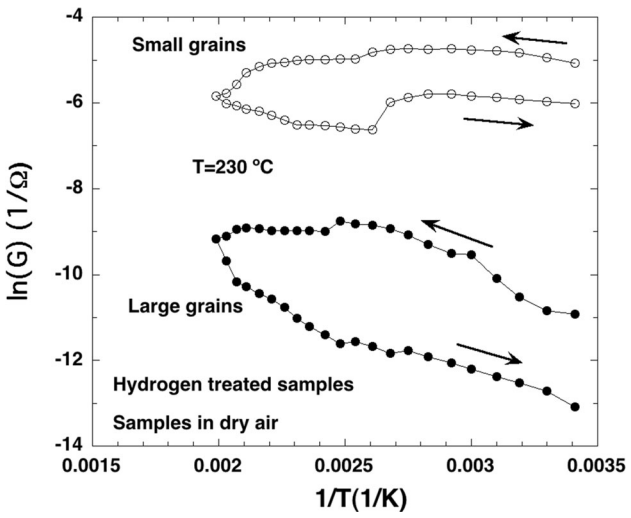

Fig. 3 Conductance during a temperature cycle, from room temperature up to 230 °C, for films SG and LG after the hydrogen treatment at 450 °C

conductance with very small temperature dependence. Along the whole cycle, the resistance changes within a range relatively small, 160–686 Ω. Also, the SG films conductance would be expected to be lower than that of LG as smaller grains imply a larger number of interfaces, and there is a noticeable change in conductivity around 110 °C. In order to elucidate the reason behind these findings, we carried out a careful study using Raman and XRD characterization.

XRD and Raman studies

Figure 4 shows the effect of treatments in a reducing atmosphere on XRD patterns of SG (small grains) and LG (large grains) SnO_2 films. Figure 4a and b show the XRD patterns of the original films, whereas Fig. 4c and d show those after treatment at 450 °C for 4 h in a N_2 atmosphere containing 5 % of H_2. In their original state, the chemical composition and crystal structure of SG and LG films match very well that of tetragonal rutile SnO_2. Most of the observed peaks correspond to the diffraction planes typical of the SnO_2 cassiterite phase (PDF n° 01-071-0652). The diffractograms also show others minor peaks that can be attributed to the substrate (alumina, PDF n° 00-011-0661) and the titanium layer (Ti_2O, PDF n° 01-73-1582). Overall, the diffraction peaks in Fig. 4b are more intense than in Fig. 4a indicating that the LG film has a better crystal quality than SG. The Scherrer formula was employed to calculate the average grain size for the films, yielding values of 53 nm for SG and 180 nm for LG. These values are in fairly good agreement with those obtained from SEM images.

XRD peak patterns show several changes after treatment with H_2 at 450 °C, as seen in Fig. 4c and d. One remarkable feature is the appearance of peaks that reveal the presence of metallic tin in both, SG and LG films (β-Sn, PDF n°00-004-0673). We also observe a decrease in

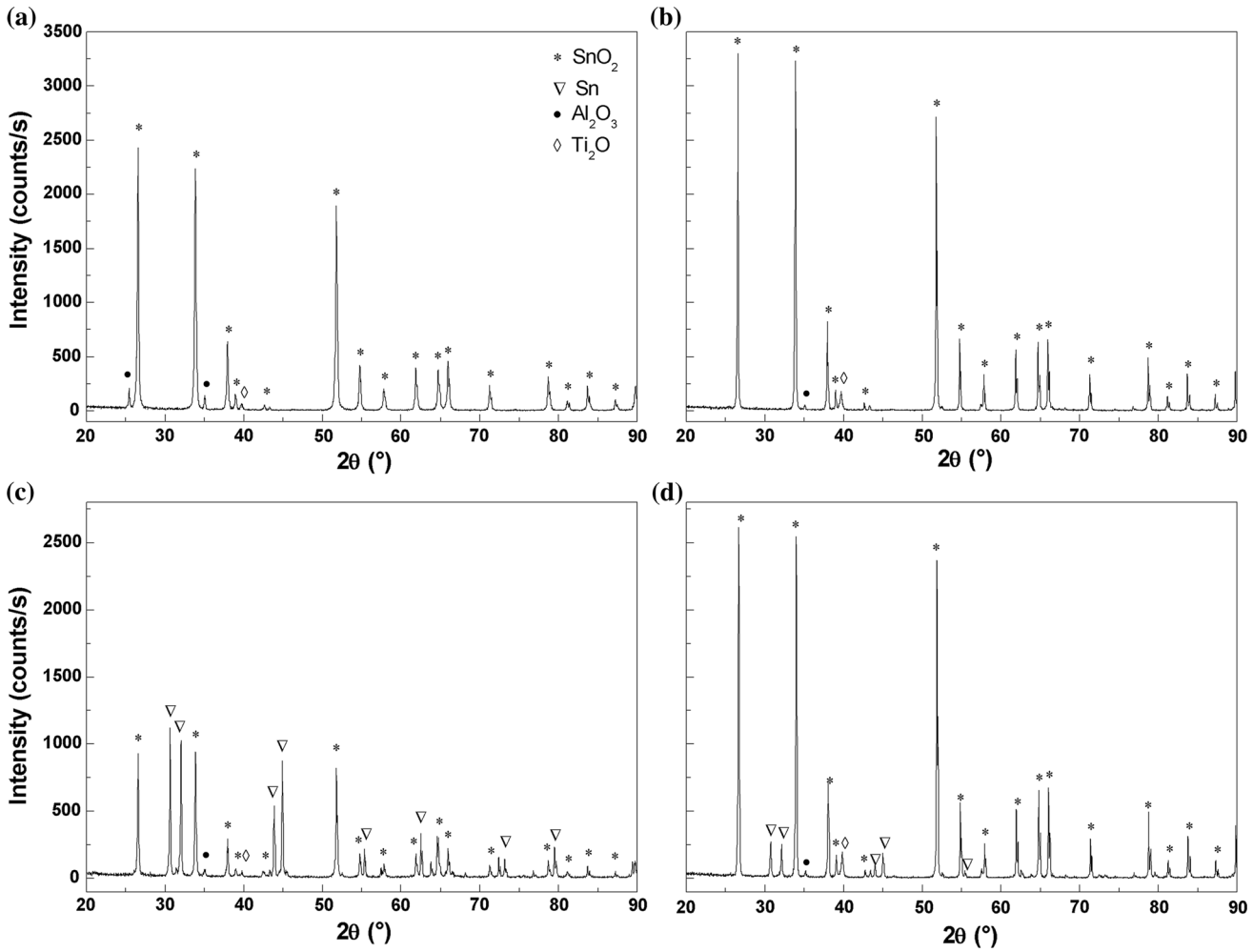

Fig. 4 XRD patterns of SG film (**a**) and LG film (**b**) after thermal treated in dry air atmosphere up to 380 °C (initial characterization), and SG film (**c**) and LG film (**d**) in a N_2 atmosphere with 5 % H_2

overall intensity of SnO_2 peaks in comparison with the original films. This decrease is particularly marked in SG, where the XRD pattern appears dominated by peaks of metallic Sn, while peaks of SnO_2 show up as a minor contribution. On the contrary, in film LG, the peaks of SnO_2 are the dominant ones and those assigned to metallic Sn appear as a minor contribution. These features indicate that the ability of reduction by H_2 depends on the grain size observing that for films with larger grain size (LG), the extent of reduction, as measured by the amount of metallic tin formed, seems to have occurred in lower degree.

Figure 5a and b shows Raman spectra for SG and LG films at the initial state, and Fig. 5c and d after treatment with H_2. Overall, the spectral window shown, covering Raman shifts between 100 and 1000 cm^{-1}, is sensitive to changes in crystal structure at several levels. The 100–400 cm^{-1} region reflects changes in oxidation state of metals and optical phonons associated with lattice vibrations where the position, width, and intensity of Raman peaks give information about the electronic configuration of the atoms and/or the lattice dynamics and structure [19]. The 400–900 cm^{-1} region consists of the classical modes related to evolution of crystallinity and nanocrystal size. Raman spectra of Fig. 5a and b correspond to the original films. Both films show Raman bands characteristics of SnO_2. Peaks at 470, 632, and 777 cm^{-1} have been assigned to the E_g, A_{1g}, and B_{2g} vibrational modes of SnO_2 in tetragonal rutile structure, respectively [20, 21]. The peak at 632 cm^{-1} (A_{1g} mode) appears shifted toward higher wavenumbers (blue shift) in the film with larger particle size, as was seen by Sangeetha and co-workers [22]. The blue shift of this peak with the increase in grain size, observed by Sangeetha, is related to size effect, suggesting a relaxation in the interface surface what makes the lattice of the grains more regular. Moreover, it may suggest a low concentration of defects at surface sites, such as oxygen vacancies. The overall Raman intensity of SnO_2 vibrational modes of the LG film, Fig. 5b, are larger than those of the SG film, Fig. 5a, which indicates that the grain size of the film influences the film crystallinity. At this point, the

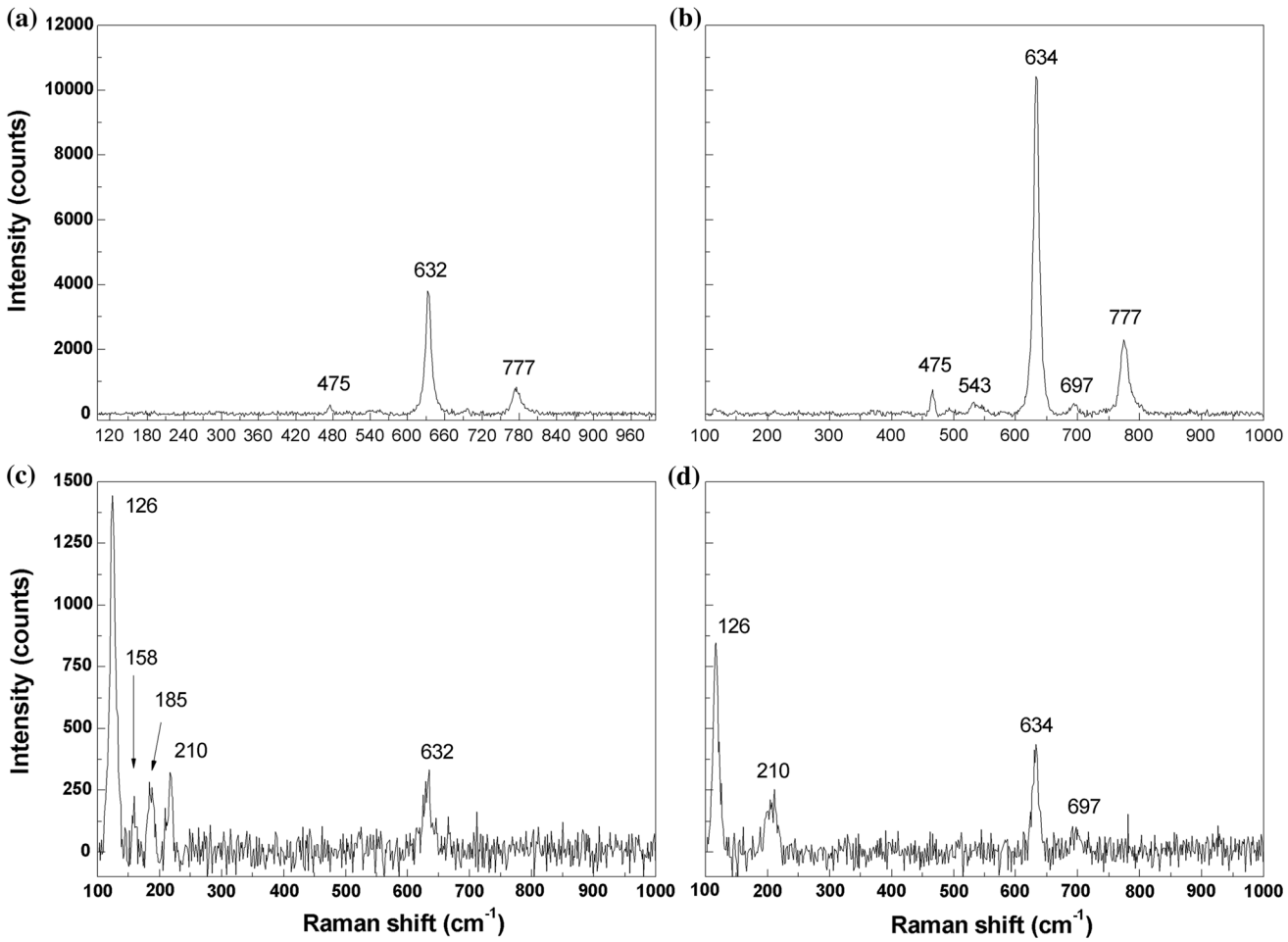

Fig. 5 Raman spectra for SG film (**a**) and LG film (**b**) after thermal treatment in dry air atmosphere up to 380 °C (initial characterization), and for SG film (**c**) and LG film (**d**) in a N_2 atmosphere with 5 % H_2

results of Raman spectroscopy are consistent with those obtained by XRD.

There are two other peaks in the Raman spectra, those at 543 and 697 cm^{-1}, which are not usually observed in bulk SnO_2 [23, 24]. These peaks may be related to new characteristic modes arising from either vacant sites or local lattice disorder [25]. Imperfections at the particle surface are likely to distort the local symmetry. This may result in the appearance of unexpected modes along with the other phonon modes associated with the deep particle core [26]. The main feature of the band at 543 cm^{-1} can be associated with surface vibrational modes of SnO_2 grains or appears because of vibrational modes of atoms bound at the particle surface. Moreover, the typical active modes of SnO_2 become better resolved in the spectrum of Fig. 5b. The peak at 697 cm^{-1} can be assigned to the so-called Raman-forbidden A_{2u} mode. This is a non-regular mode, called "surface mode," and is associated with the increase in surface area due to the nanoparticle structure. Abello et al. [27] suggest that the Raman activity of this mode is induced by disorder.

The Raman spectra after treatment in reductive atmosphere are shown in Fig. 5c and d. Compared with the spectra before H_2 treatment, we observe a rather dramatic decrease in overall intensity and the appearance of a new set of Raman bands in the 100-400 cm^{-1} spectral region. Intensities of peaks associated to SnO_2 are largely reduced in both films although peak positions remained invariant, including the blue shift observed in LG. Raman peaks at 126 and 210 cm^{-1} are observed in both films. The peak at 126 cm^{-1} is consistent with the high-energy Raman peak in metallic β-Sn [28] thus confirming the results anticipated by XRD. However, the peak at 210 cm^{-1} corresponds to a SnO phase [28, 29], not detected by XRD. At this point, we should consider that the energy of the incident photons arising from a 514 nm laser beam (2.4 eV) is very close to the energy gap of SnO ($E_{g\ SnO} = 2.5$–3 eV) so Raman enhancement by resonant effect is expected [29]. It may well explain the fact that we observe Raman scattering even from very small amounts of SnO that actually cannot be detected by XRD. On the other hand, we do not expect resonant Raman enhancement in SnO_2 as its energy gap, 3.6 eV, appears a bit far from the energy of the incident photon, so any of the peaks attributed to SnO_2 arise from a conventional Raman scattering mechanism.

The Raman spectrum of the SG film after reduction, Fig. 5c, reveals two other peaks at 158 and 185 cm^{-1}, intermediate to those at 126 and 210 cm^{-1} just described. Notice that these peaks are absent in the LG film, see Fig. 5d. These peaks at 158 and 185 cm^{-1} can be attributed to a transition oxides SnO_x where $1 < x < 2$ [29, 30]. This intermediate and specific phase, ascribed to a sub-stoichiometric SnO_x, was also observed by Sangaletti and coworkers [31] from oxidation studies of SnO films in steps to SnO_2. These authors found that the Raman spectrum displayed two intense and sharp peaks between 145 and 185 cm^{-1} that can not be assigned to SnO or SnO_2. Respective XRD measurements showed reflections ascribed to a SnO_x suboxide with x ranging from 1.33 to 1.5, allowing us to attribute the Raman bands accordingly.

The same films subjected to reduction with hydrogen were then exposed to oxygen atmosphere at 450 °C and then analyzed. XRD patterns are shown in Fig. 6a and b. The film with smaller grain size, SG, shows diffraction peaks attributed to several species. The dominant phase can be assigned to the tetragonal phase of cassiterite SnO_2, indicating that the metallic tin has been reverted to SnO_2 (PDF n° 01-071-0652). This transformation is not complete as many characteristic peaks of β-Sn are still observed (PDF n° 00-004-0673). Furthermore, the diffraction pattern reveals the presence of tin oxides with lower oxidation state such as SnO (PDF n° 01-072-1012) or Sn_2O_3 (PDF n° 01-072-1012), and intermediate tin oxide phase that has been reported to appear at elevated temperatures [14]. In this intermediate oxide, tin is present between SnO and SnO_2 as a mixture of Sn(II) and Sn(IV). The XRD pattern of the LG film, Fig. 6b, reflects a much more uniform chemical composition as most of the peaks observed solely correspond to a SnO_2 phase (PDF n° 01-071-0652), indicating that almost all of the metal tin was converted to tin dioxide.

The Raman spectra of the reduced and later oxidized samples are shown in Fig. 7a and b. As observed in XRD, the Raman spectrum of the SG film shows a much more rich spectral pattern than that of LG, with several peaks in the low wavenumber region (126, 138, 170, 185, 210, and 631 cm^{-1}). The peak at 126 cm^{-1} is very weak and corresponds to remaining metallic tin whereas the peak at 210 cm^{-1}, previously earlier assigned to SnO, appears as a shoulder. The peak at 631 cm^{-1}, corresponding to the SnO_2 phase, is certainly minor. Remarkably, the major peaks observed in the spectrum, for instance those at 138 and 170 cm^{-1}, are consistent with the existence of well-defined intermediates tin oxide phases [29, 30]. Two new peaks, at 185 and 221 cm^{-1}, can be assigned to other intermediate oxide, Sn_2O_3 [32]. Raman results confirm that oxidation of an initially reduced SnO_2 film with smaller grain size generates several intermediate tin oxides, as observed by XRD. In marked contrast, the Raman spectrum of Fig. 7b, that of the film with larger grain size, is almost totally dominated by peaks of SnO_2. Although some other minor peaks are observed in the spectrum, consistent with the presence of tiny amounts of metallic tin and SnO, the structure of the LG film is essentially that of the SnO_2 phase, in total agreement with the XRD analysis.

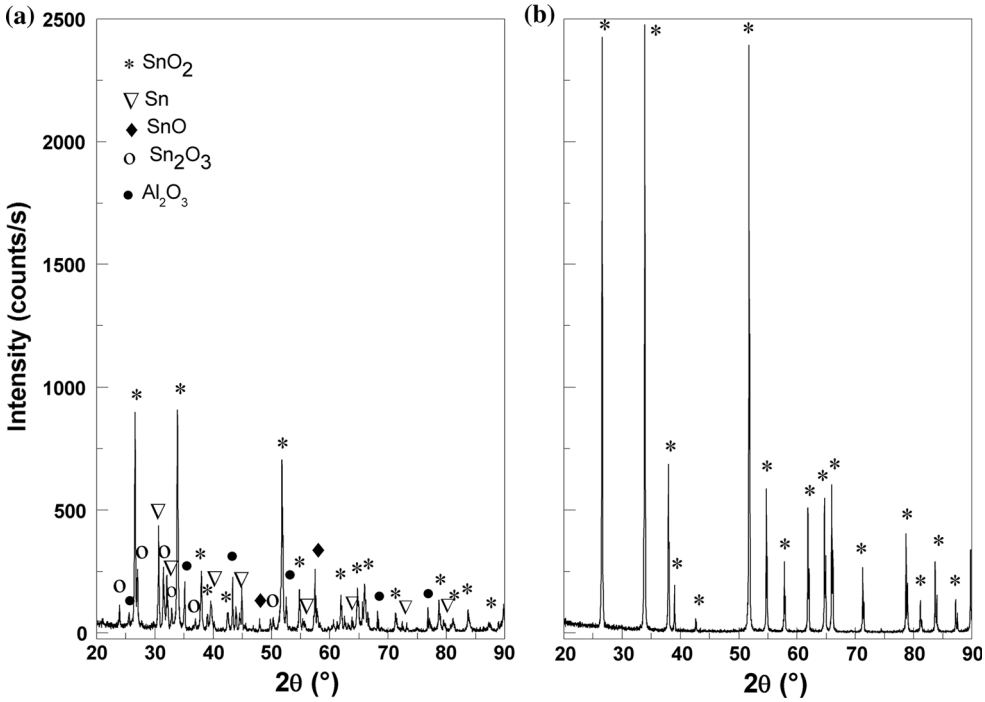

Fig. 6 XRD patterns in oxygen atmosphere after hydrogen treatment of SG (**a**) and LG (**b**) films at 450 °C

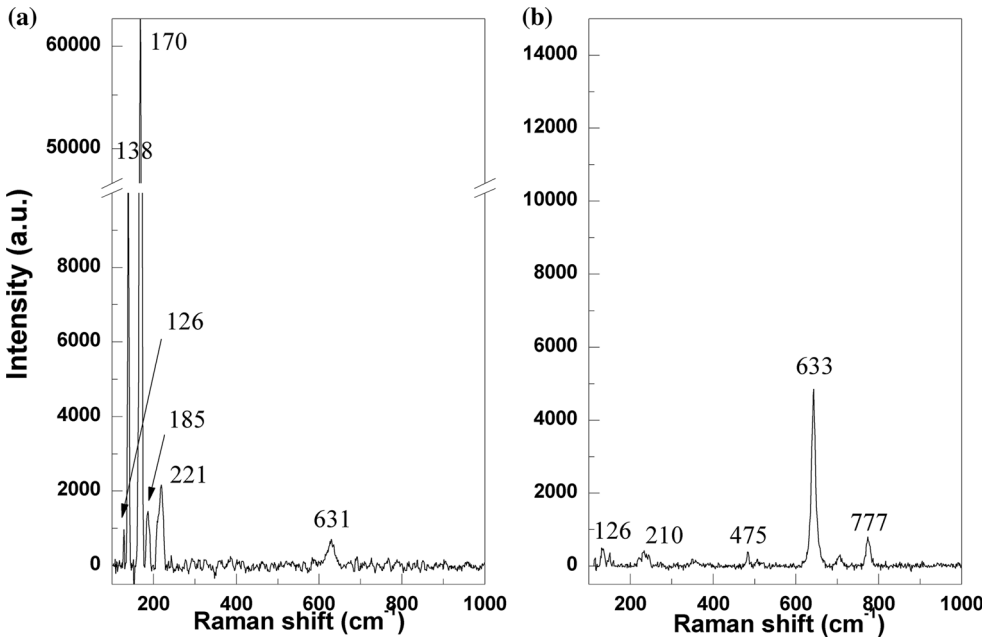

Fig. 7 Raman spectra in oxygen atmosphere after hydrogen treatment for SG (**a**) and LG (**b**) films at 450 °C

In summary, XRD and Raman reveal that after treatment with H_2 at 450 °C, SnO_2 is reduced to metallic Sn and SnO, plus other intermediate oxides. The extent of this reduction depends on the grain size; the smaller the grain size the larger the amount of metallic tin. The subsequent oxidation of the treated films reverts this reduction but in a degree that markedly depends on grain size. Whereas in the films with LG the dominant phase is SnO_2, the film with smaller grain shows the appearance of several intermediate oxides.

Let us put these results in perspective with earlier work. We have recently reported studies on SnO_2 films thermally treated in H_2 atmospheres up to 350 °C, where XPS analysis did not reveal the presence of metallic Sn phases [16]. Overall, XPS results showed that exposing the SnO_2 samples to reducing environments does not modify the chemical composition of the film, which appears in contradiction with our observations here on the presence of metallic Sn, and several intermediate oxides with oxidation

state lower than IV. The difference between experiments is that the temperature of the reductive treatments was higher here (450 °C) than earlier (350 °C). As a sort of confirmation, we also analyzed SnO_2 films subjected to reductive treatments at lower temperatures using the combination of Raman and XRD techniques (results not shown). Reaffirming the results obtained by XPS, no traces of Sn or intermediate oxides were found.

When a metal oxide based sensor is exposed to air, O_2 adsorbs on the surface of the material. Due to oxygen adsorption, oxygen molecules trap electrons from the conduction band of the material because of strong electronegativity of the oxygen atom and hence induces oxygen adsorption [33]. Below 150 °C oxygen adsorption at the surface is mainly in form of O_2^- while above this temperature chemisorbed oxygen in form of O^- or O^{2-} is found [14]. Tharsika et al. [33] suggests that O^{2-} ion is the only species stable at temperatures above 300 °C. Sadek and co-workers [34] stated that when the sample is exposed to hydrogen, it reacts with the chemisorbed oxygen and produces H_2O, which is expressed in Eq. (4):

$$H_2 + O^{2-}_{(ads)} \rightarrow H_2O_{(g)} + 2e^-. \quad (4)$$

This reaction takes place at the surface of the material, and no change in the chemical composition of the metal oxide-based sensor was reported, maybe due to the low-tested exposure times. Contrary, in the present study, we suggest that the reduction of SnO_2 by hydrogen at 450 °C could occur through two different paths. One reaction could be the complete reduction of SnO_2 to metallic tin:

$$SnO_2 + 2H_2 \rightarrow Sn + 2H_2O. \quad (5)$$

The second possibility is the formation of SnO by an incomplete reduction of SnO_2, as a result of the following reaction:

$$SnO_2 + H_2 \rightarrow SnO + H_2O. \quad (6)$$

Once SnO is produced at temperatures greater than 380 °C, the dismutation of this species in Sn and SnO_2 could happen through the following reaction [35]:

$$2SnO \leftrightarrow SnO_2 + Sn, \quad (7)$$

which explains the presence of metallic tin found with Raman and XRD techniques. Also, Geurts et al. [29] suggest that the dismutation starts by the displacement of the internal oxygen at lower temperatures:

$$xSnO \leftrightarrow SnO_x + (x-1)Sn \quad (8)$$

For a comparison, even though the XRD data for a specific grain size shows similar intensities of SnO_2 phase after H_2 and O_2 treatment (Figs. 4c and 6a for SG, and Figs. 4d and 6b for LG film), the oxidation process occurs. This is evident because the intensity of the main SnO_2 Raman peak increases after the oxidation process. However, it could be possible that the SnO_2 obtained after this reaction is at an amorphous state and not crystallizes in the tetragonal phase of cassiterite. It is important to note that the increase of the intensity of the main SnO_2 Raman peak of the LG film after O_2 treatment is much more evident than the increase for the SG film. This feature indicates that the oxidation process for the large particles is more complete than for the small ones. This could be due to the presence of larger amount of metallic tin before the oxidation process for the small particles size and the slower conversion rate from Sn to stannous and stannic ions. The dynamics of the oxidation process is expected to be controlled by the diffusion of oxygen within the lattice. Consequently, at higher temperatures, external oxygen can diffuse into the lattice and finally oxidizes the metallic tin and the intermediate SnO_x to the highest possible oxidation state, namely SnO_2. As is shown in Fig. 7, the observed peaks of the intermediate oxides SnO_x in SG film have a very high intensity. This suggests that in the small particles grain size there is a great accumulation of SnO_x that cannot oxidize to SnO_2, and these intermediate oxides show a resonance enhancement of the Raman scattering.

Electrical measurements interpretation

It has long been recognized that Schottky barriers at grain surfaces determine the resistance of this type of gas sensors. Therefore, the key issues are barrier formation at intergrains and electron transport between grains. Conduction mechanisms have been regularly interpreted in analogy to those in metal–semiconductor contact diodes. Accordingly, the electrical properties of polycrystalline semiconductors are usually described with a simple one-dimensional model representing the interface between two grains. Figure 8a depicts the double Schottky barrier model that is generally accepted. It is regularly considered that a thermionic mechanism (TE) is responsible for the sample conductivity, which is described by Eq. (1). However, it has been pointed out that quantum–mechanical tunneling through the barrier can be present for the regular barriers characteristics. At low temperatures and for heavily doped semiconductors, the main contribution to electrical conduction arises from tunneling of electrons with energies close to the Fermi energy in the semiconductor; this is known as the field emission, case FE in Fig. 8a. As the temperature is raised or for not so highly doped semiconductors, only electrons with enough energy can tunnel the barriers as they "see" a lower and thinner barriers, case TFE in Fig. 8a. The thermionic mechanism depends only on intergranular barrier heights while electron-tunneling

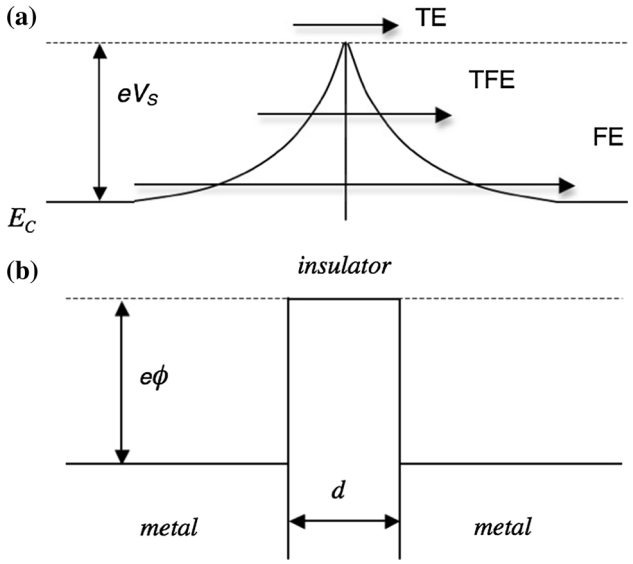

Fig. 8 **a** Depicts a double Schottky barrier of height eVs. Possible conduction mechanisms are thermionic emission (TE), thermionic field emission (TFE), and field emission (FE). **b** Depicts a metal–insulator-metal system or MIM diode

mechanisms depend both on intergranular barrier heights and widths.

After the hydrogen treatment, we determined that SnO_2 was converted to SnO (onto the film surface) and Sn, and also for SG in a much larger degree than LG samples. Then, we expect a complex behavior for LG films, with the presence of SnO_2 and SnO, and regions with amorphous Sn and then a very high conductivity. In the case of SG films, Raman and XRD results indicated an important conversion into Sn after their exposure to hydrogen. Since the samples are exposed to oxygen during measurements, oxygen can form a thin oxide layer and adsorb at the intergrains. Thus, conduction between grains does not correspond any longer to that of a polycrystalline semiconductor but to a polycrystalline metal with thin insulating layers in between. Therefore, we can expect that the electrical conductance between grains resembles that of a metal–insulator–metal system or MIM diode having a narrow insulating film corresponding to the oxidized intergrain. Figure 8b shows a simple diagram of a MIM diode. The conduction mechanism of this system is quantum–mechanical tunneling through the thin oxide layer of width *d*. As for field emission in Schottky diodes, the conductivity in this type of diodes presents a low dependence on temperature, especially for the barrier heights that are typical in tin oxide [36].

Based on the above analysis, we conclude that the temperature response of SG films of Fig. 3 basically reflects the conductivity between grains, which conform a MIM diode. This explains the large conductivity values and the low temperature dependence. The insulating layer oxygen could include adsorbed species. Thus, the conductance change observed at about 110 °C could be due to a conversion of adsorbed oxygen species. Indeed, at low temperatures the dominant oxygen species is O_2^-, while at relatively high temperatures the dominant species is O^-. This mechanism implies an increase in intergranular barriers at high temperature, reducing the conductivity.

Conclusions

SnO_2-thick films with two different grain sizes were prepared onto alumina substrate that were delineated by sputtering with an interdigitated shape. The overall Raman intensity of SnO_2 vibrational modes of the LG film suggest a low concentration of defects on the surface sites, such of oxygen vacancies, and a better crystal quality. Also, it was found by Raman spectroscopy and XRD that the ability of reduction and oxidation depends on the grain size of the films. For films with smaller grain size, the extent of reduction, as measured by the amount of metallic tin, appeared to occur in more degree. After the oxidation process, the dominant phase in SG films could be assigned to cassiterite, indicating that the metallic tin has been reverted to SnO_2. However, this transformation was not complete as many characteristic peaks of metallic tin and intermediate oxides were still observed. In marked contrast, for larger grain particles (LG), a much more uniform chemical composition of SnO_2 was found. Considering the electrical measurements, results for SG samples showed a conductance with very small temperature dependence. This behavior corresponds to a metal–insulator–metal system or MIM diode, having a narrow insulating film corresponding to the oxidized intergrain.

Acknowledgements This work was partially supported by the ANPCyT (Agencia Nacional de Promoción Científica y Tecnológica, Argentina).

References

1. Yamazoe N (2005) Toward innovations of gas sensor technology. Sens Actuators B 108:2–14
2. Gopel W, Schierbaum KD (1995) SnO2 sensors: current status and future prospects. Sens Actuators B 26:1–12
3. Barsan N, Weimar U (2001) Conduction model of metal oxide gas sensors. J Electroceram 7:143–167
4. Cukrov LM, McCormick PG, Galatsis K, Wlodarski W (2001) Gas sensing properties of nanosized tin oxide synthesised by mechanochemical processing. Sens Actuators B 77:491–495
5. Mad MJ, Morrison R (1989) Chemical sensing with solid state devices, vol 1. Academic Press, San Diego
6. Romppainen P, Lantto V (1988) The effect of microstructure on the height of potential energy barriers in porous tin dioxide gas sensors. J Appl Phys 63:5159–5165

7. Maffeis TGG, Owen GT, Malagu C, Martinelli G, Kennedy MK, Kruis FE, Wilks SP (2004) Direct evidence of the dependence of surface state density on the size of SnO_2 nanoparticles observed by scanning tunnelling spectroscopy. Surf Sci 550:21–25
8. Kamp B, Merkle R, Maier J (2001) Chemical diffusion of oxygen in tin dioxide. Sens Actuators B 77:534–542
9. Ponce MA, Castro MS, Aldao CM (2009) Capacitance and resistance measurements of SnO_2 thick-films. J Mater Sci 20:25–32
10. Maffeıs TGG, Owen GT, Malagu C, Martinelli G, Kennedy MK, Kruis FE, Wilks SP (2004) Direct evidence of the dependence of surface state density on the size of SnO 2 nanoparticles observed by scanning tunnelling spectroscopy. Surf Sci 550(1):21–25
11. Malagù C, Martinelli G, Ponce MA, Aldao CM (2008) Unpinning of the Fermi level and tunneling in metal oxide semiconductors. Appl Phys Lett 92:162104
12. I.I.C.f.D. (1998) Data, powder diffraction file database, Newtown Square, EEUU
13. Sahm T, Gurlo A, Bârsan N, Weimar U (2006) Basics of oxygen and SnO2 interaction; work function change and conductivity measurements. Sens Actuators B 118:78–83
14. Batzill M, Diebold U (2005) The surface and materials science of tin oxide. Prog Surf Sci 79:47–154
15. Aldao CM, Schipani F, Ponce MA, Joanni E, Williams FJ (2014) Conductivity in SnO2 polycrystalline thick film gas sensors: tunneling electron transport and oxygen diffusion. Sens Actuators B 193:428–433
16. Schipani F, Ponce MA, Joanni E, Williams FJ, Aldao CM (2014) Study of the oxygen vacancies changes in SnO2 polycrystalline thick films using impedance and photoemission spectroscopies. J Appl Phys 116:194502
17. Ponce MA, Castro MS, Aldao CM (2004) Influence of oxygen adsorption and diffusion on the overlapping of intergranular potential barriers in SnO2 thick films. Mater Sci Eng B 111:14–19
18. Aldao CM, Mirabella DA, Ponce MA, Giberti A, Malagù C (2011) Role of intragrain oxygen diffusion in polycrystalline tin oxide conductivity. J Appl Phys 109:063723
19. Vijayarangamuthu K, Rath S (2014) Nanoparticle size, oxidation state, and sensing response of tin oxide nanopowders using Raman spectroscopy. J Alloy Compd 610:706–712
20. Wang JX, Liu DF, Yan XQ, Yuan HJ, Ci LJ, Zhou ZP, Gao Y, Song L, Liu LF, Zhou WY, Wang G, Xie SS (2004) Growth of SnO2 nanowires with uniform branched structures. Solid State Commun 130:89–94
21. Ristić M, Ivanda M, Popović S, Musić S (2002) Dependence of nanocrystalline SnO2 particle size on synthesis route. J Non-Cryst Solids 303:270–280
22. Sangeetha P, Sasirekha V, Ramakrishnan V (2011) Micro-Raman investigation of tin dioxide nanostructured material based on annealing effect. J Raman Spectrosc 42:1634–1639
23. Sun SH, Meng GW, Zhang GX, Gao T, Geng BY, Zhang LD, Zuo J (2003) Raman scattering study of rutile SnO2 nanobelts synthesized by thermal evaporation of Sn powders. Chem Phys Lett 376:103–107
24. Meier C, Lüttjohann S, Kravets VG, Nienhaus H, Lorke A, Ifeacho P, Wiggers H, Schulz C, Kennedy MK, Kruis FE (2006) Vibrational and defect states in SnOx nanoparticles. J Appl Phys 99:113108
25. Berengue OM, Simon RA, Chiquito AJ, Dalmaschio CJ, Leite ER, Guerreiro HA, Guimarães FEG (2010) Semiconducting Sn3O4 nanobelts: growth and electronic structure. J Appl Phys 107:033717
26. Aragón FH, Coaquira JAH, Hidalgo P, da Silva SW, Brito SLM, Gouvêa D, Morais PC (2011) Evidences of the evolution from solid solution to surface segregation in Ni-doped SnO2 nanoparticles using Raman spectroscopy. J Raman Spectrosc 42:1081–1086
27. Abello L, Bochu B, Gaskov A, Koudryavtseva S, Lucazeau G, Roumyantseva M (1998) Structural Characterization of Nanocrystalline SnO2 by X-Ray and Raman Spectroscopy. J Solid State Chem 135:78–85
28. Mcguire K, Pan ZW, Wang ZL, Milkie D, Menendez J, Rao AM (2002) Raman studies of semiconducting oxide nanobelts. J Nanosci Nanotechnol 2(5):499–502
29. Geurts J, Rau S, Richter W, Schmitte FJ (1984) SnO films and their oxidation to SnO2: Raman scattering, IR reflectivity and X-ray diffraction studies. Thin Solid Films 121:217–225
30. Arunkumar.PBS, Satyanarayana L, Manorama SV (2012) One-pot hydrothermal synthesis of SnO and SnO_2 nanostructures: enhanced H2 sensing attributed to in situ p-n junctions. In: IMCS (ed) The 14th international meeting on chemical sensors, pp 372–375
31. Sangaletti L, Depero LE, Allieri B, Pioselli F, Comini E, Sberveglieri G, Zocchi M (1998) Oxidation of Sn Thin Films to SnO2. Diffraction Studies. J Mater Res 13:2457–2460
32. Chen X, Grandbois M (2013) Insitu Raman spectroscopic observation of sequential hydrolysis of stannous chloride to abhurite, hydroromarchite, and romarchite. J Raman Spectrosc 44:501–506
33. Tharsika T, Haseeb ASMA, Akbar SA, Sabri MFM, Wong YH (2015) Gas sensing properties of zinc stannate (Zn_2SnO_4) nanowires prepared by carbon assisted thermal evaporation process. J Alloy Compd 618:455–462
34. Sadek AZ, Choopun S, Wlodarski W, Ippolito SJ, Kalantar-zadeh K (2007) Characterization of ZnO nanobelt-based gas sensor for H 2, NO 2, and hydrocarbon sensing. IEEE Sens J 7(6):919–924
35. Molloy KC, Quill K, Cunningham D, McArdle P, Higgins T (1989) A reinvestigation of the structures of organotin sulphates and chromates, including the crystal and molecular structure of bis (trimethyltin) sulphate dihydrate. J Chem Soc Dalton Trans 2:267–273
36. Grover S, Moddel G (2013) Metal single-insulator and multi-insulator diodes for rectenna solar cells. In: Grover S, Moddel G (eds) Rectenna solar cells. Springer, New York